Three-stage oxidation kinetics and passivation mechanism of spark plasma sintered ZrC ultra-high temperature ceramic

Lin, Yun Ching; Brouwer, Hans; Popovich, Vera; Tang, Yinglu

DOI
10.1016/j.jeurceramsoc.2025.117757

Publication date
2026

Document Version
Final published version

Published in
Journal of the European Ceramic Society

Citation (APA)
Lin, Y. C., Brouwer, H., Popovich, V., & Tang, Y. (2026). Three-stage oxidation kinetics and passivation mechanism of spark plasma sintered ZrC ultra-high temperature ceramic. *Journal of the European Ceramic Society*, *46*(2), Article 117757. https://doi.org/10.1016/j.jeurceramsoc.2025.117757

Journal of the European Ceramic Society 46 (2026) 117757

Contents lists available at ScienceDirect

Journal of the European Ceramic Society

journal homepage: www.elsevier.com/locate/jeurceramsoc

Three-stage oxidation kinetics and passivation mechanism of spark plasma sintered ZrC ultra-high temperature ceramic

Yun-Ching Lin [a,*], Hans Brouwer [b], Vera Popovich [b], Yinglu Tang [a,*]

[a] Faculty of Aerospace Engineering, Department of Aerospace Structures and Materials, Delft University of Technology, Kluyverweg 1, Delft 2629 HS, the Netherlands
[b] Faculty of Mechanical Engineering, Department of Materials Science and Engineering, Delft University of Technology, Mekelweg 2, Delft 2628 CD, the Netherlands

ARTICLE INFO

Keywords:
Zirconium Carbide (ZrC)
Ultra-High Temperature Ceramic (UHTC)
Paralinear oxidation kinetics
Activation energy
Passivation mechanism

ABSTRACT

ZrC Ultra-High Temperature Ceramic is a promising material for future extreme environment applications. However, its susceptibility to oxidation at elevated temperatures poses a significant challenge. There remains unresolved controversy in literature regarding its oxidation kinetics and activation energies. The temperature, oxygen pressure and time effects on the oxidation and passivation of ZrC are still not fully understood. To address these questions, we fabricated near-stoichiometric ZrC ceramic via spark plasma sintering (SPS) and for the first time investigated the temperature-oxygen pressure-time (T-P-t) dependent oxidation kinetics of SPS-sintered ZrC. A three-stage oxidation mechanism including a passivation stage was reported. The study also revealed the complexity of activation energy dependence on temperature and pressure within the 3D T-P-t space. Additionally, it uncovered the conditions necessary to maintain the passivation of ZrC. These findings provide valuable insights for future design of oxidation-resistant ZrC and carbides, paving the way for advancements in materials for extremes.

1. Introduction

Zirconium Carbide (ZrC) Ultra-High Temperature Ceramic (UHTC) possesses excellent mechanical and thermal properties such as high hardness (25 GPa) and high congruent melting point up to 3700 K due to the mixed ionic and covalent bonding. In addition, ZrC has a lower cost in comparison with other UHTCs. These properties render ZrC a promising material for future extreme environment applications [1–3]. However, its susceptibility to oxidation at elevated temperatures for instance above 500 °C [4] remains a major issue. The oxidation response can compromise the structural integrity of ZrC-based materials during high-temperature applications involving air exposure. Consequently, it is essential to evaluate the potential oxidation damage to ZrC UHTC.

The oxidation reaction of ZrC is a complicated heterogenous reaction and its kinetics can be affected by factors such as temperature, oxygen pressure and exposed duration. Additionally, the oxidation kinetics of ZrC can also be affected by sample properties, which include purity, relative density, grain size, surface roughness, surface area, and C/Zr stoichiometry [5,6], stemming from different preparation methods. ZrC in different forms, for example single crystal [7,8], powder [9,10], and sintered pellets [11,12], can also affect the oxidation response. Due to the convoluted factors mentioned above, literature controversies on the oxidation rate constants and resultant activation energies (E_a) prevail despite the various experiments conducted.

Bartlett et al. [13] studied the oxidation of powdered ZrC at 450–580 °C in 6.5×10^{-3}–100 % O_2 and presumed two parallel controlling processes. One process was the predominant surface reaction occurring at the ZrC-ZrO_2 phase boundary that accounted for most of the oxidation with E_a of 192.5 kJ/mol. The other process was believed to be a separate but parallel process of oxygen diffusion through the oxide scale into the ZrC lattice replacing C in the initial stages, with E_a of 221.7 kJ/mol. The diffusion process, however, could not be observed at oxygen pressure below 5×10^{-3} atm, which was attributed to residual C hampering the concentration gradient to induce continued diffusion of C out of the lattice.

Barnier et al. [14] fixed the oxygen pressure to be 10 % O_2 but extended the temperature range to 400–1000 °C, and reported that E_a in the beginning of oxidation of ZrC powder was 292 kJ/mol controlled by diffusion and then changed to 186 kJ/mol controlled by surface reaction as the oxidation reaction fraction exceeds 0.20. The energy barrier for diffusion is much larger compared to that of Bartlett, but E_a for surface reaction is in good agreement between the two studies.

---

[*] Corresponding authors.
E-mail addresses: Y.Lin-4@tudelft.nl (Y.-C. Lin), Y.Tang-5@tudelft.nl (Y. Tang).

https://doi.org/10.1016/j.jeurceramsoc.2025.117757
Received 1 April 2025; Received in revised form 13 August 2025; Accepted 18 August 2025

Shimada et al. [9] reported the isothermal oxidation of ZrC powders in 380–600 °C under oxygen pressures of 1.3, 2.6, or 7.9 % O_2 with flowing argon. The kinetics was described by diffusion-controlled Jander's equation [9] (see Eq. 1):

$$\left[1-(1-\alpha)^{\frac{1}{3}}\right]^2 = kt \tag{1}$$

where α is the reacted fraction at time t, and k is the rate constant that depends on temperature and pressure. The oxygen bulk diffusion through a coherent ZrO_2 layer was considered to be the rate-determining step. Two E_a were obtained with 138 kJ/mol below 470 °C and 180 kJ/mol above that temperature, of which the transition was attributed to the formation of cubic ZrO_2 accompanied by the generation of cracks. The E_a values are smaller compared to those of Bartlett [13] and Barnier [14].

Similarly, Rao et al. [15] reported the oxidation kinetics of ZrC powder under 20 % O_2 in temperature range of 477–537 °C with E_a of 131.8 kJ/mol. Different E_a were reported with non-isothermal conditions in the temperature range of 277–1027 °C. E_a were reported to have a large oxygen pressure dependence, with values ranging from 142.3 to 126.7–99.8 kJ/mol at oxygen pressures of 5, 20, and 50 % O_2.

Kuriakose and Margrave [16] investigated the oxidation of electron beam melted ZrC pellet in the temperature range of 554–652 °C. The oxygen pressure used in the experiments was 97 % O_2. The result showed that the oxidation followed a linear rate law controlled by chemical reaction with E_a of 70.1 kJ/mol.

Gasparrini et al. [17] studied the oxidation of hot-pressed ZrC cuboids in 21 % O_2 in the temperature range of 800–1100 °C. Linear kinetics was reported at 800 °C, and for temperatures above 800 °C, oxidation was linear up to 7200 s followed by an accelerated breakaway oxidation.

Konnik et al. [18,19] investigated the mass gain of hot-pressed ZrC via flow-tube furnace under 1000–1600 °C at 20 % O_2. They observed when oxidation elapsed time increased, the lower temperature regime began to dominate in total mass increase, which pointed to a relative slowdown in oxidation at higher temperatures. They reported that kinetic, morphological, and microstructural deviations across temperatures were the major contributors to mass gain behavior of ZrC.

Table 1 summarizes the types of ZrC, oxidation temperatures, oxygen pressures, oxidation kinetics, and E_a reported by various authors. It is noteworthy that there are inconsistencies and even contradictions in different findings, and three core questions regarding the oxidation kinetics of ZrC UHTC remain to be answered. One is the existence range of a diffusion-controlled protective parabolic oxidation stage of ZrC. Another is the reason for the transition of parabolic to linear oxidation and the conditions at which it occurs. The other is the E_a of ZrC oxidation and its dependence on temperature profile, oxygen pressure, and oxidation time.

Aiming at answering these questions, we fabricated sintered stoichiometric ZrC ceramic (C/Zr ≈ 1) and investigated its oxidation kinetics under a wide range of temperatures and oxygen pressures. ZrC ceramic was made via SPS due to several advantages including reduction of sintering duration, uniform distribution of heat, and high densification compared to other sintering techniques [20–22]. With controlled density and purity, the oxidation behavior of stoichiometric SPS-sintered ZrC was studied under varying temperatures 600–1000 °C, oxygen pressures 2–21 % O_2, and elapsed time up to 10800 s. A consistent comparison was performed across different parameter ranges in 3D T-P-t plots. Instead of the commonly assumed linear oxidation of ZrC, a passivation stage was discovered and the reason for parabolic-to-linear oxidation rate transition was also uncovered. Furthermore, the E_a of ZrC UHTC oxidation as a function of oxygen pressure and temperature was derived. These findings could build a foundation for designing future oxidation-resistant ZrC materials as well as other carbide ceramics.

2. Materials and methods

2.1. Material fabrication

ZrC ceramic disk (C/Zr ≈ 1) was synthesized using solely ZrC powder (purity: 99.5 %, particle size < 45 μm, Goodfellow, UK) as the starting material. ZrC powder was placed in a 30 mm diameter graphite die within a glovebox to minimize oxygen contamination. Subsequently, the graphite die containing the ZrC powder was transferred to the SPS furnace. The ZrC powder was then densified using SPS with a HP D 25 SD furnace (FCT Systeme GmbH, Germany) in a graphite die under vacuum. Two-step sintering was carried out at 1500 °C for 120 s followed by 2000 °C for 600 s under 80 MPa uniaxial pressure with a heating rate of 3.3 °C/s. The first holding step at 1500 °C was applied to reduce possible contamination during sample preparation before entering high-temperature sintering. The sintered sample was cooled to room temperature with a cooling rate of 0.4 °C/s, and the remaining

Table 1
Comparison of ZrC oxidation studies.

Type of ZrC	Temperature (°C)	O_2 pressure (% O_2)	Rate-controlling step and kinetics	E_a (kJ·mol^{-1})		Reference
Powder	450–580	6.5×10^{-3}–100	Combined phase boundary reaction and diffusion controlled	O_2 diffusion 221.7	Phase boundary reaction 192.5	Bartlett et al. [13]
Powder	400–1000	10	Diffusion controlled in the beginning and then changed to surface reaction controlled as the oxidation reaction fraction exceeds 0.20	O_2 diffusion 292	Surface reaction 186	Barnier et al. [14]
Powder	380–600	1.3 2.6 7.9	Diffusion-controlled Jander's equation	Below 470 °C 138	Above 470 °C 180	Shimada et al. [9]
Powder	477–537	20	Non-parabolic mechanism	131.8		Rao et al. [15]
Electron beam melted (99.5 % purity)	554–652	97	Chemical reaction controlled; Linear	70.1		Kuriakose et al. [16]
Hot-pressed (> 96 % of theoretical density)	800–1100	21	Linear	–		Gasparrini et al. [17]
Hot-pressed (99.9 % purity)	1000–1600	20	Mass gain at 1200 °C exceeded higher temperatures for elapsed time > 1200 s	–		Konnik et al. [18,19]

graphite on the surface of ZrC ceramic disk was removed with a grinder-polisher (MetaServ 250, Buehler, the USA). The phase and composition of SPS-sintered ZrC are shown in Supplementary: Figure S1 and S2.

The resulting bulk ZrC ceramic disk had a density of 6.64 ± 0.01 g/cm^3 calculated from averaging three measurements performed by the Archimedes method and a relative density of 98.7 ± 0.1 %. The ZrC ceramic disk was sanded and polished to mirror-like surface. Lastly, the ceramic disk was machined into rectangular cuboids with dimensions of approximately 6 mm × 6 mm × 3 mm utilizing cutting machine (Secotom-60, Struers, Denmark) with a diamond cut-off wheel (M1D20) to eliminate surface area effects on the oxidation kinetics.

2.2. Isothermal static oxidation

Static oxidation test was carried out by the ZrC rectangular ceramic cuboids (6 mm × 6 mm × 3 mm) placed on a crucible inside the furnace of a thermogravimetric analyzer (TGA) (Seteram TAG 16/18, Caluire, France). The crucible with ZrC ceramic cuboid was mounted at one side of the balance and an identical but empty crucible was mounted at the other side of the balance. Both furnaces, each at one side of the balance, were heated simultaneously with 0.08 °C/s in a flow of pure Ar. When both furnaces of the thermogravimetric analyser reached the target temperature, O_2 was added to the Ar gas flow with controlled oxygen pressure during the isothermal hold. The temperature and pressure ranges were: 600–1000 °C and 2.0–21.0 % O_2. Afterwards, the furnace was cooled with 0.08 °C/s cooling rate to room temperature. Interruption experiments were done under fixed oxygen pressure with Ar-2.0 % O_2 flow at 600, 700, 800, and 1000 °C. Mass change was assessed via thermogravimetric analyses, using a dual furnace balance (Seteram TAG 16/18, France) which allowed automatic correction for buoyancy effects. The analyser was equipped with Pt/Pt-10 %Rh (S-type) thermocouples. The gas mixture was admitted to the TGA analyser via mass flow controllers (Bronkhorst, The Netherlands) operated with Labview (version 2020) such that the total gas flow matched 100 sccm, which was equally divided over both furnace tubes. Prior to admitting the gas mixture to the furnace, O_2 and Ar (Linde Gas Benelux BV, purity better than 5 N) were filtered to remove residual moisture and hydrocarbons with Hydrosorb (< 20 ppb H_2O) and Accosorb (< 10 ppb hydrocarbons) filters (Messer Griesheim, Germany) respectively. Ar gas was additionally filtered to remove residual O_2 with an Oxysorb filter (< 5 ppb O_2). Samples were labelled as Zx-y-z, where x, y, z relate to temperature, oxygen pressure, and time respectively, for example Z6–2–30 (6: 600 °C, 2: 2 % O_2, 30: 3000 s). The details of the samples are shown in Table 2.

2.3. Characterization

Quadrupole Mass Spectrometry (QMS) was used to monitor the formation of gaseous CO_2 during isothermal oxidation in the TGA furnace. The microstructures and morphologies of the SPS-sintered ZrC and corresponding oxide scale were analyzed by Scanning Electron Microscopy (SEM) with a JSM-IT 100 (JEOL, Japan). Comprehensive results and supporting data from the X-ray Diffraction (XRD), Energy-Dispersive X-ray Spectroscopy (EDX), Transmission Electron Microscopy (TEM), and Raman spectroscopy analyses are presented in the Supplementary Information.

Table 2
Samples of isothermal oxidation at oxygen pressure of 2 % O_2.

Temp (°C) time (s)	600	700	800	1000
1500	–	Z7–2–15	Z8–2–15	Z10–2–15
3000	Z6–2–30	Z7–2–30	–	–
5400	–	Z7–2–54	–	–
10800	Z6–2–108	Z7–2–108	Z8–2–108	Z10–2–108

2.4. Oxidation kinetics

Based on the weight change curve over time from TGA data and the CO_2 formation curve from QMS data, three possible oxidation stages were identified.

1. Stage one oxidation (k_1 parabolic oxidation)

   From the moment oxygen was turned on to the beginning of CO_2 signal increase captured by QMS. Based on the evidence obtained from TEM-EDX elemental mapping, Selected Area Electron Diffraction (SAED) (see Supplementary: Figure S3), and QMS, the predominant oxidation reaction mechanism occurring in stage one was proposed to proceed via one or both of the following pathways:

   $$ZrC + \frac{1}{2}(1-x)O_{2(g)} \rightarrow ZrC_xO_{1-x} + (1-x)C \tag{2}$$

   $$ZrC + \frac{1}{2}(2-x)O_{2(g)} \rightarrow ZrO_{2-x} + C \tag{3}$$

   Selected Area Electron Diffraction Pattern (SAEDP) (see Supplementary: Figure S3 (f)) revealed that the crack-free oxide scale contained a substantial amount of amorphous carbon, which supported the proposed predominant reaction mechanisms. Furthermore, in this stage, only a limited amount of CO_2 was detected by QMS. These findings collectively indicated that the predominant oxidation reaction involved the formation of amorphous carbon with minimal carbon oxidation, which resulted in significant carbon retention within the compact oxide scale.

   A parabolic fitting was used (see Eq. 4) in stage one oxidation.

   $$\left(\frac{\Delta w}{w_0}\right)^2 = k_1 t + c \tag{4}$$

   where Δw is the weight change, w_0 is the initial weight, k_1 is the parabolic rate constant, and c is an integration constant.
2. Stage two oxidation (k_2 intermediate oxidation)

   From the time CO_2 surged to the saturation of CO_2 release, a general parabolic fitting was used (see Eq. 5). In this stage, carbon oxidation $C + O_{2(g)} \rightarrow CO_{2(g)}$ started to pick up, which was detected by QMS.

   $$\left(\frac{\Delta w}{w_0}\right)^2 + \alpha\left(\frac{\Delta w}{w_0}\right) = k_2 t + c \tag{5}$$

   where Δw is the weight change, w_0 is the initial weight, k_2 is the parabolic rate constant, $\frac{k_2}{\alpha}$ is the linear rate constant in stage two oxidation, and c is an integration constant.

   The general parabolic oxidation equation suggested that stage two oxidation involved a combination of parabolic and linear kinetics, indicating a transitional regime between parabolic and linear oxidation behavior.
3. Stage three oxidation (k_3 linear oxidation)

   From the saturation of the CO_2 release, a linear fitting was used (see Eq. 6).

   $$\left(\frac{\Delta w}{w_0}\right) = k_3 t + c \tag{6}$$

   where Δw is the weight change, w_0 is the initial weight, k_3 is the linear rate constant, and c is an integration constant.

   All three stages of ZrC oxidation were fitted with R^2 values above 0.99. The following Table 3 presents the definitions of the terms employed throughout the study.

Table 3

Terminology and definitions.

Terminology	Definition
In-plane cracks	The cracks which propagate parallel to the nominal surface of the pristine ZrC substrate, extending laterally within the oxide scale
Through-thickness cracks	The cracks which propagate perpendicular to the nominal surface of the pristine ZrC substrate, extending through the thickness of the oxide scale
Inner layer	The compact oxide layer which is directly bonded to the ZrC substrate
Outer layer	The cracked oxide layer which is positioned with one side in contact with the inner layer while the opposite side exposed to the atmosphere
Parabolic stage	The oxidation stages during which the kinetics conform to parabolic fitting (Eq. 4) or general parabolic fitting (Eq. 5)
Full protectiveness	The capacity of an oxide scale to significantly inhibit further oxidation, characterized by ZrC oxidation kinetics that conform to a parabolic rate law, as determined by parabolic fitting (Eq. 4) of experimental data
Partial protectiveness	The condition in which the oxide scale provides limited resistance to oxidation, characterized by ZrC oxidation kinetics that conform to a general parabolic rate law, as determined by general parabolic fitting (Eq. 5) of experimental data
Non-protectiveness	The absence of effective resistance to oxidation, characterized by ZrC oxidation kinetics that conform to a linear rate law, as determined by linear fitting (Eq. 6) of experimental data

3. Results and discussion

3.1. Three-stage paralinear oxidation kinetics

3.1.1. Existence of parabolic stage and its dependence on temperature

By fixing the oxygen pressure to 2 % O_2 and isothermal oxidation time to 10800 s, the oxidation stages during isothermal oxidation at different temperatures (600–1000 °C) were investigated. At 600 °C isothermal oxidation, two parabolic stages were identified. In the first stage (before *point a* in Fig. 1(a)), a decline in CO_2 formation was identified in QMS, and the limited CO_2 formation was in agreement with a compact scale (thickness: 3.85 ± 0.49 μm) (Fig. 1(b)). In the second stage (after *point a* in Fig. 1(a)), prominent CO_2 formation was detected by QMS concurrently with the appearance of a double-layer scale formation (Fig. 1(c)). While the inner layer (thickness: 3.37 ± 1.24 μm) remained compact, there was increased amount of through-thickness cracks (with reference to the nominal surface of the pristine ZrC substrate) in the outer layer as observed in Fig. 1(c). Despite the existence of some through-thickness cracks, the overall oxidation rate at 600 °C was continuously decreasing throughout the entire elapsed time, which indicated no linear oxidation stage at 600 °C up to isothermal oxidation duration 10800 s. Parabolic (Eq. 4) and general parabolic (Eq. 5) fittings were applied to the two respective oxidation stages. Based on these results, it was concluded that ZrC followed a parabolic oxide scale growth behavior under 2 % O_2 up to 10800 s.

At 700 °C isothermal oxidation, a compact oxide layer with a thickness of 15.05 ± 0.93 μm was observed (Fig. 2(b)) when isothermal oxidation time was 1500 s. As CO_2 formation started to rise, so was the number of through-thickness cracks in the outer layer of oxide scale (Fig. 2(c)), which was similar to the observation at 600 °C. In addition, in-plane cracks (with reference to the nominal surface of the pristine ZrC substrate) were also observed due to the stresses from ZrO_2 grain growth. Starting from isothermal oxidation time 5400 s (*point c* in Fig. 2 (a)), the derivative of normalized weight gain remained constant, which indicated a linear k_3 oxidation stage confirmed with a compact inner layer of constant thickness (10.07 ± 1.74 μm) and linearly growing outer layer with cracks (Fig. 2(d) and (e)). This is coherent with the observation and analysis of Shimada [23]. To conclude, at 700 °C, although a compact inner layer was observed at the end of the isothermal oxidation process (10800 s), the outer cracked layer exhibited linear growth. This behavior resulted in overall oxidation kinetics that followed a linear rate law from isothermal oxidation time 5400 s onward.

At 800 °C isothermal oxidation, the CO_2 release rate rapidly spiked up without the initial decline as observed at 600 °C and 700 °C. The missing of k_1 oxidation stage indicated a lack of compact oxide scale. The as-observed oxide scale exhibited a higher crack density compared to those formed at 600 °C and 700 °C. In-plane cracks, accompanied by a limited number of through-thickness cracks were observed during the initial stage of oxide scale formation (Fig. 3(b)). Significant through-thickness cracks, which extended through the scale completely, were observed at a later stage (Fig. 3(c)). The ZrO_2 grain growth increased the stress between the oxide and carbide, which resulted in enhanced in-plane crack formation. Despite the formation of significant in-plane cracks, the occurrence of through-thickness cracks caused by carbon oxidation remained limited as shown in Fig. 3(b). The scale, despite exhibiting limited through-thickness cracks, functioned as a barrier layer that effectively impeded significant inward oxygen diffusion to the fresh ZrC surface, as evidenced by the TGA curve. Consequently, the oxidation kinetics remained parabolic. This stage (before *point a* in Fig. 3 (a)) was defined as the k_2 stage, which was fitted with a general parabolic equation (Eq. 5). When the through-thickness cracks propagated through the oxide scale completely, linear k_3 oxidation took place and ZrC was no longer resistant to oxidation. In addition, maltese cross scale formation was observed at 10800 s, with oxide spallation occurring at the edges of the ZrC substrate (Fig. 3(c)). This is consistent with the phenomenon reported by Gasparrini et al. [24]. Edge oxide spallation resulting from maltese cross shape formation may be another factor which facilitated the onset of linear oxidation, which promoted k_2 to k_3 oxidation stage.

At 1000 °C isothermal oxidation, similarly to 800 °C, CO_2 formed rapidly, as depicted in Fig. 4(a). A major difference in ZrC oxidation at around 1000 °C compared to lower temperatures were the observed pronounced cracks along the grain boundaries (GB), as can be seen in Fig. 4(b)(c)(d). This was most likely due to GB diffusion of oxygen and subsequent carbon reaction into CO_2. The release of CO_2 gas during carbon oxidation caused extensive cracking at the grain boundaries, which ultimately led to oxide scale spallation. Significant amount of carbon retention in ZrC after being oxidized at 1000 °C in the k_2 stage was found from Raman spectrum (see Supplementary: green spectrum in Figure S4). This retained carbon was also identified by Gasparrini [17], and was reported to contribute to a reduction in the oxidation rate at 1000 °C and 1100 °C. When the grain boundaries near the surface were thoroughly penetrated by CO_2 release, as shown in Fig. 4(c), oxidation transitioned to linear k_3 oxidation kinetics.

By plotting the isothermal oxidation TGA curves of different temperatures at 2 % O_2, it was found that as the oxidation temperature increased, the weight gain increased drastically which can be seen in Fig. 5.

3.1.2. Oxidation stage dependence on temperature, oxygen pressure, and time

By repeating the experiments done at 2 % O_2 to other oxygen pressures (see Supplementary: Figure S5 (a)(b)(c)), we constructed three-dimensional contour plots illustrating different oxidation stages over a range of temperatures (T), oxygen pressures (P), and isothermal oxidation durations (t) within the T-P-t space. Additionally, the 3D T-P-t space was visualized through two-dimensional t-P projections (Fig. 6), as explained below.

(1) Compact scale formation in the k_1 parabolic stage

Oxidation kinetics in the k_1 stage followed parabolic rate law according to TGA curves, which indicated oxygen diffusion through the

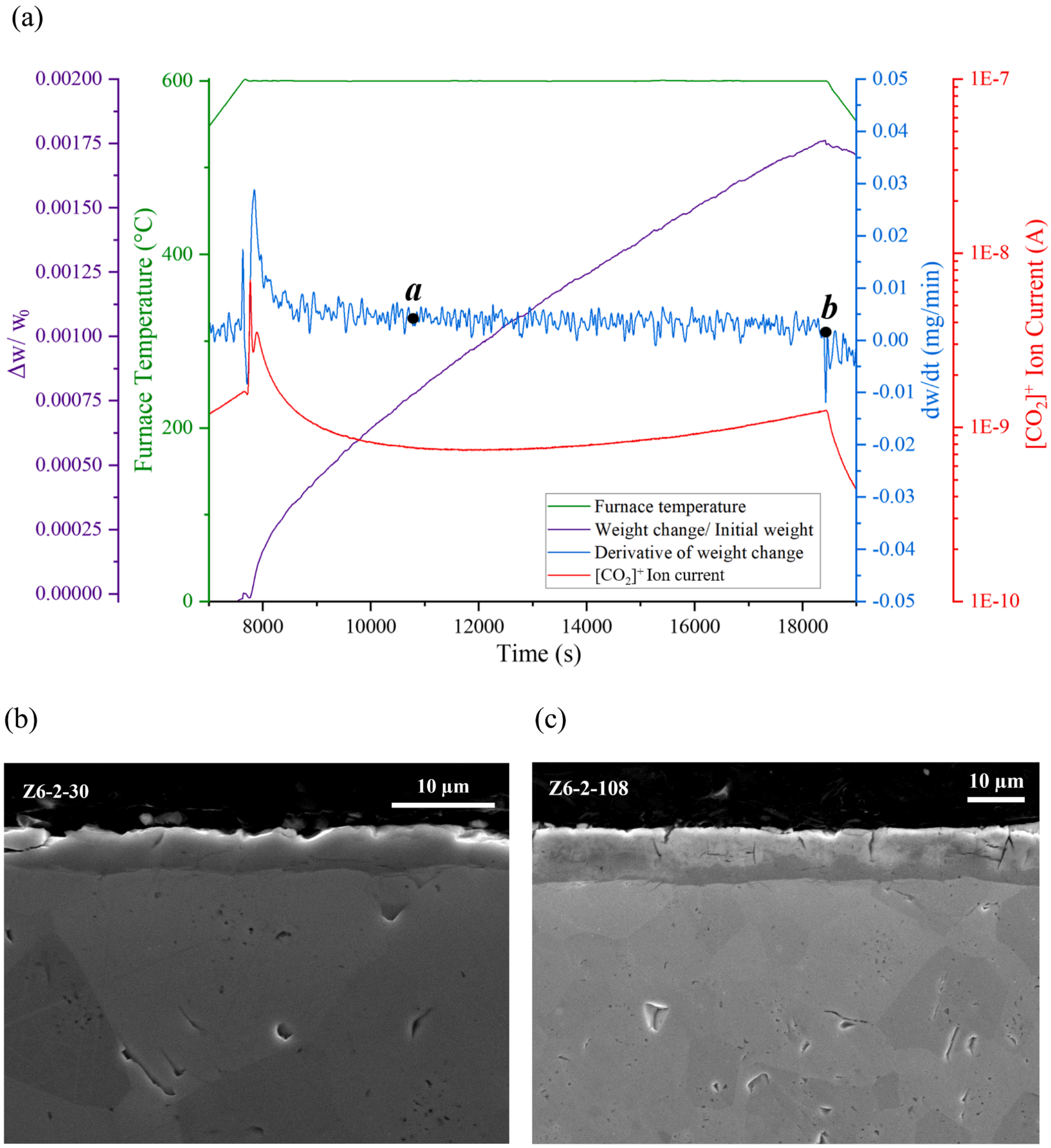

Fig. 1. (a) TGA-QMS graph of SPS-sintered ZrC oxidized at 600 °C under 2 % O_2 for 10800 s. Point a: Z6–2–30; point b: Z6–2–108. 2 % O_2 was introduced when the TGA furnace reached 600 °C. Time zero of the graph is set as the moment pure Ar gas valve is on. (b) Cross-sectional SEM image of Z6–2–30 (point a). (c) Cross-sectional SEM image of Z6–2–108 (point b).

oxide film as the rate-controlling process. Moreover, low CO_2 signal was identified by QMS from the moment the oxygen valve was opened to *point a* in Fig. 1(a) and Fig. 2(a). Low CO_2 formation indicated a high carbon retention in the compact layer, as confirmed by Raman spectroscopy (see Supplementary: Figure S6), and reduced the risk of through-thickness crack formation. This was confirmed in SEM images where few cracks were observed in the compact layer. A dense zirconia oxide layer enriched with amorphous carbon (see Supplementary: Figure S6 and Figure S7) hindered further O inward diffusion and was considered to be the reason of the full protectiveness in the blue T-P-t space in Fig. 6(a).

(2) Incomplete through-thickness / GB crack formation in the k_2 intermediate stage

In the k_2 stage, a surge of CO_2 emission was identified from QMS, which led to the formation of limited through-thickness or GB cracks which had not yet traversed the scale completely. Thus, diffusion through the oxide scale still played a role in the overall oxidation mechanism and contributed to the partial protectiveness in the orange T-P-t space in Fig. 6(c). The full-protective blue space (Fig. 6(a)) and partial-protective orange space (Fig. 6(c)) jointly comprised the overall protective green T-P-t space in Fig. 6(e). Kinetics results reported by Shiro Shimada et al. [9] and Barnier et al. [14] which showed parabolic oxidation fell into the green T-P-t space albeit their relatively small elapsed time compared to what was investigated in this study.

(3) Complete through-thickness / GB crack formation in the k_3 linear stage

Oxidation kinetics in the k_3 stage followed linear rate law according to TGA curves, indicating instead of diffusion, chemical reaction became the rate-limiting step. In addition, CO_2 QMS signal reached saturation (after *point c* in Fig. 2(a); after *point a* in Fig. 3(a) and Fig. 4(a)). The continuous CO_2 formation led to substantial formation of through-thickness or grain boundary cracks contingent on temperature

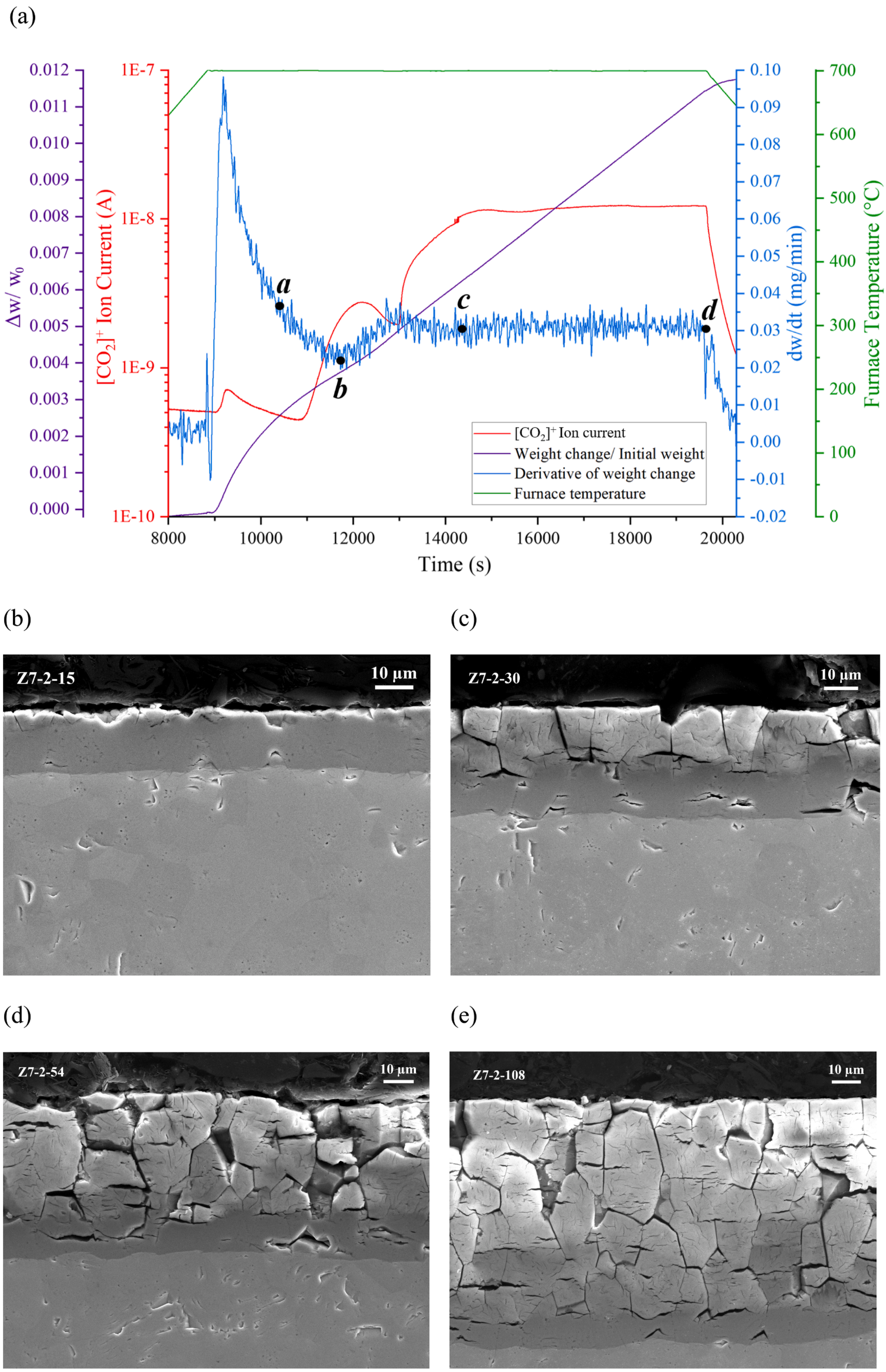

Fig. 2. (a) TGA-QMS graph of SPS-sintered ZrC oxidized at 700 °C under 2 % O_2 for 10800 s. Point a: Z7–2–15; point b: Z7–2–30; point c: Z7–2–54; point d: Z7–2–108. 2 % O_2 was introduced when the TGA furnace reached 700 °C. Time zero of the graph is set as the moment pure Ar gas valve is on. Cross-sectional SEM images: (b) Z7–2–15 (point a); (c) Z7–2–30 (point b); (d) Z7–2–54 (point c); (e) Z7–2–108 (point d).

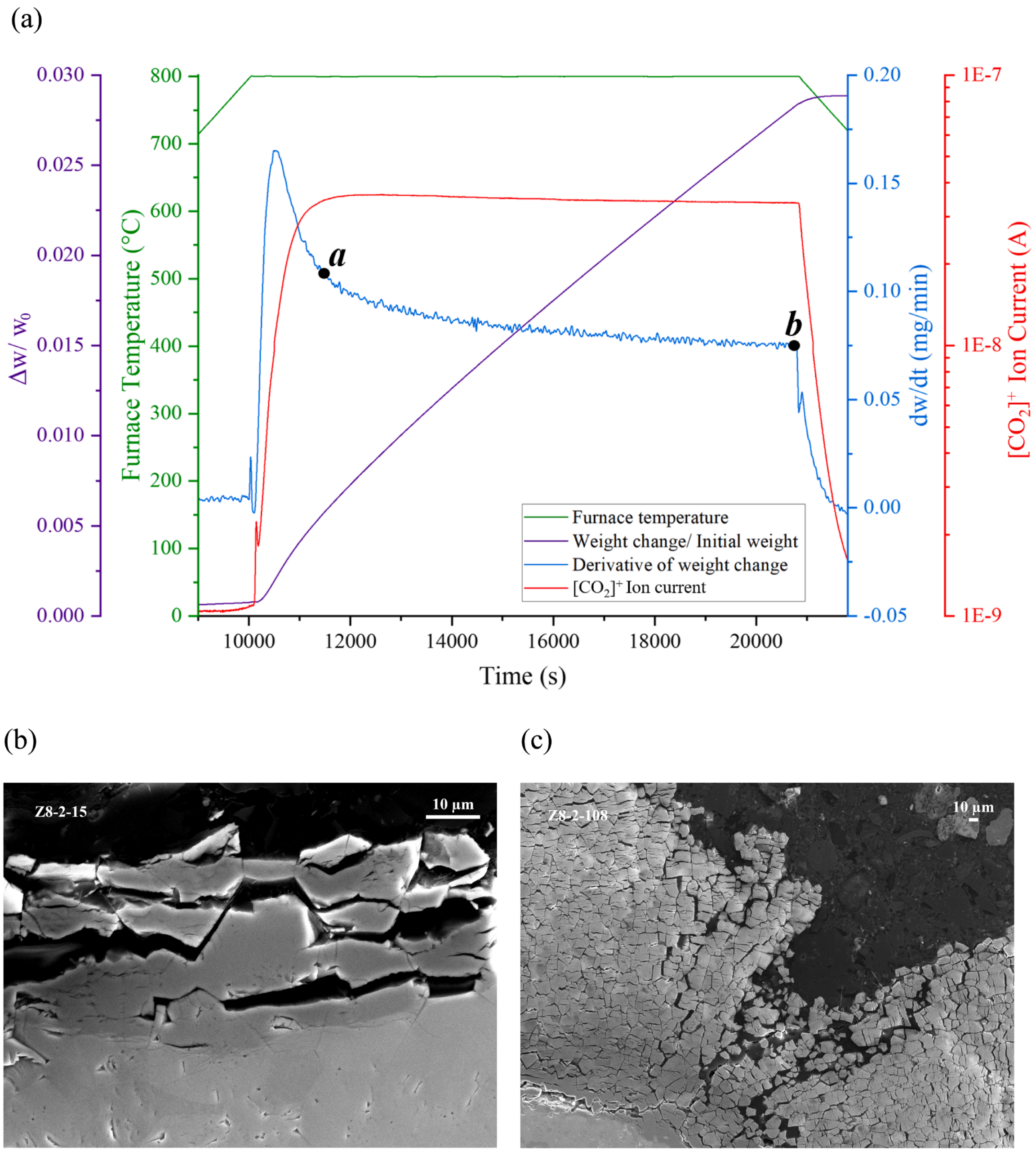

Fig. 3. (a) TGA-QMS graph of SPS-sintered ZrC oxidized at 800 °C under 2 % O_2 for 10800 s. Point a: Z8–2–15; point b: Z8–2–108. 2 % O_2 was introduced when the TGA furnace reacheed 800 °C. Time zero of the graph is set as the moment pure Ar gas valve is on. (b) Cross-sectional SEM image of Z8–2–15 (point a). (c) Cross-sectional SEM image of Z8–2–108 (point b) showing the edge oxide spallation from maltese cross shape formation.

conditions. For instance, at temperatures below 1000 °C, complete through-thickness cracks were observed in SEM (Fig. 2(e) and Fig. 3(c)). When the temperature was at 1000 °C, complete GB cracks were identified which were shown in Fig. 4(c). Both indicated the loss of partial protectiveness in the k_3 stage (T-P-t space outside green region in Fig. 6 (e)). Kinetics results reported by Rao et al. [15] and Gasparrini et al. [17] which exhibited linear oxidation fell in the non-protective T-P-t space.

To maintain the overall protectiveness of ZrC against oxidation, confining the temperature, oxygen pressure, and oxidation duration within the green T-P-t space in Fig. 6(e) is suggested to avoid linear oxidation. It is noted that the higher the oxidation temperature and oxygen pressure, the smaller the protective range in terms of oxidation duration. The influence of oxygen pressure on oxidation rate is further discussed in the section below.

3.1.3. Oxidation rate dependence on oxygen pressure

By plotting rate constant against oxygen pressure with Eq. 7, the oxidation rate dependence on oxygen pressure was investigated.

$$lnk = m \bullet \ln PO_2 + c \tag{7}$$

where k is the oxidation rate constant, m is the coefficient, PO_2 is the oxygen pressure, and c is a constant.

Oxidation rate was found to be independent of oxygen pressure in the temperature range 600–700 °C for k_1 and 600–800 °C for k_2, which could be due to diffusion being the rate-determining step [13]. By interrupting the oxidation experiment in these stages, the composition of the as-formed oxide layer was investigated. XRD patterns confirmed the existence of ZrO_2, and Raman spectra further confirmed that besides ZrO_2, the oxide scale contained a significant quantity of carbon in an

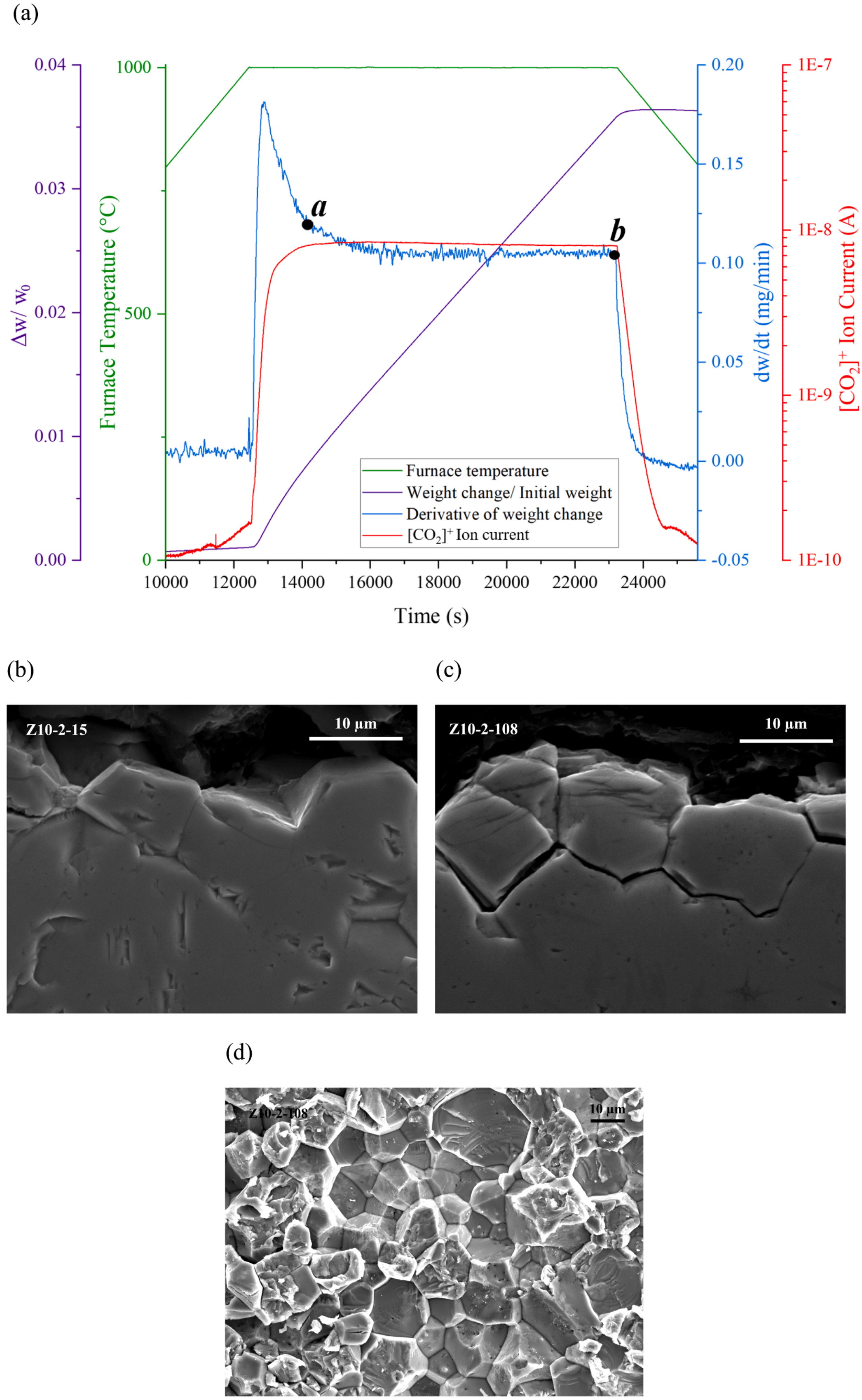

Fig. 4. (a) TGA-QMS graph of SPS-sintered ZrC oxidized at 1000 °C under 2 % O_2 for 10800 s. Point a: Z10–2–15; point b: Z10–2–108. 2 % O_2 was introduced when the TGA furnace reached 1000 °C. Time zero of the graph is set as the moment pure Ar gas valve is on. (b) Cross-sectional SEM image of Z10–2–15 (point a). (c) Cross-sectional SEM image of Z10–2–108 (point b). (d) Top-view SEM image of Z10–2–108 (point b).

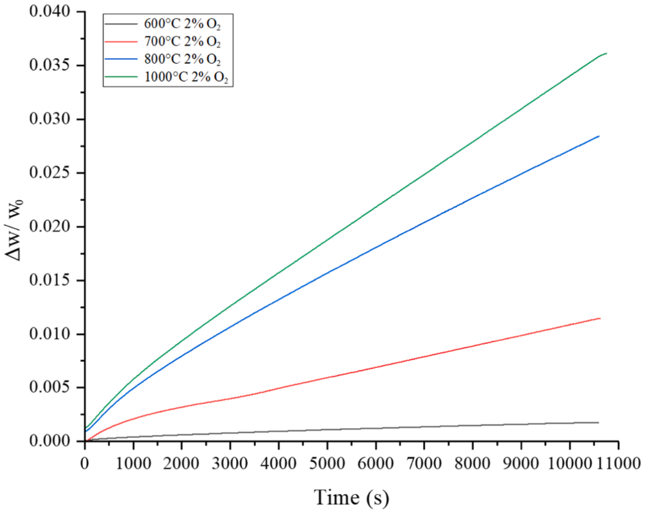

Fig. 5. Isothermal oxidation TGA curves at 2 % O_2 in temperature range 600–1000 °C. Time zero of the isothermal oxidation TGA curves is set as the moment 2 % O_2 is introduced to the furnace.

amorphous state (see Supplementary: Figure S4, S6, S7, and S8). A O/Zr ratio less than 2 with C content approximately 20–50 at. percent (at%) in k_1 and k_2 stage at temperatures below 1000 °C was found via in SEM-EDX (see Supplementary: Table S1, Table S2, and Table S3). The oxygen deficiency indicated the possibility of oxygen transport through oxygen vacancies. According to Kofstad [25], when oxygen deficit of the compact oxide scale remains, the parabolic oxidation rate constant merely scales with the oxygen diffusion coefficient at substrate-oxide interface and is independent on the oxygen pressure, which agrees well with the observations shown in Fig. 7(a). Nevertheless, the dependence on oxygen pressure (m= 0.97) was observed when temperature reached 1000 °C for k_2. It is speculated that, given the fact pronounced GB penetration observed at high-temperature oxidation, as can be seen in Fig. 4(c)(d), the higher oxygen pressure could favor the transport of molecular oxygen into the grain boundaries.

In the k_3 stage, the rate constants were all dependent on oxygen pressure, which showed a power law dependence of k_3 with respect to oxygen pressure. The coefficient m values were 0.29, 0.62, 0.77 for 700 °C, 800 °C, 1000 °C respectively. Significant formation of through-thickness or grain boundary cracks led to a strong dependence of the rate constant on ambient oxygen pressure. The direct proportionality of $\ln k_3$ to $\ln PO_2$ further indicated that molecular oxygen transport and adsorption onto the surface via short circuits became increasingly important, while oxygen vacancy diffusion no longer played a crucial role in oxygen transport. Meanwhile, chemical reaction by the oxidation of ZrC became the rate-controlling step rather than oxygen diffusion through the oxide scale. The oxidation rate constants under different temperatures and oxygen pressures are summarized in Table 4.

3.2. Activation energy dependence on oxygen pressure and temperature

The activation energies were calculated using Arrhenius equation (see Eq. 8).

$$k = A \cdot e^{\left(-\frac{E_a}{RT}\right)} \tag{8}$$

where k is the overall oxidation reaction rate constant, A is the pre-exponential factor, E_a is the energy of activation, R is the universal gas constant, and T is the temperature. The value of E_a was calculated using slope and intercept of lnk versus 1/T in the abovementioned temperature range. The Arrhenius plots of k_1, k_2, and k_3 rate constants can be found in Fig. 8. The observations from the activation energies (shown in Table 5) are as follows:

(1) Continuous reduction of E_a values from k_1, k_2, and to k_3 stages.

Continuous crack formation due to CO_2 formation was observed when oxidation entered the k_2 and k_3 stages. In the k_1 stage, compact oxide scale offered protection against oxygen diffusion. The increased crack density resulted in a decrease in E_a during the k_2 stage. In the k_3 stage, the fully cracked outer oxide scale rendered the E_a no longer diffusion-controlled, but instead governed by the kinetics of chemical reactions. The reduction of E_a when the rate-limiting step shifted from diffusion to chemical reaction was in agreement with the observation by Bartlett et al. [13] and Barnier et al. [14].

(2) A turning point at 800 °C observed in both k_2 and k_3 stages.

In the k_2 stage, since the partial cracks compromised the protectiveness of the oxide scale, the turning point at 800 °C was likely due to the fact that the origin of cracks were formed by significant GB diffusion above 800 °C, leading to cracking along grain boundaries, which was observed in both cross-sectional and top-view SEM images (Fig. 4(c)(d)). These cracks above 800 °C exhibited a completely different morphology from those below 800 °C. In the k_3 stage, although at all temperatures, completely cracked oxide scales were observed, above 800 °C, scale spallation was much more severe in comparison with that at lower temperatures. This may be the reason for a further reduced E_a.

(3) E_a independence on oxygen pressure in the k_1 stage.

This energy barrier arose from the oxygen self-diffusion at the carbide-oxide interface and was independent of oxygen pressure. The oxygen-pressure-independent E_a was coherent with what was found in Section 1.3. The values of E_a in the k_1 stage averaged to 252.2 kJ/mol, which was close to E_a reported by Bartlett [13] with 221.7 kJ/mol under temperature range of 450–580 °C, and Barnier [14] with 292 kJ/mol under 400–1000 °C in the diffusion-controlled steps.

(4) E_a dependence on oxygen pressure in the k_2 and k_3 stages.

As oxygen pressure increases, E_a was found to increase as well. High oxygen pressure is believed to impede the escape and release of CO_2 from the scale across all temperatures in both the k_2 and k_3 stages, during which the CO_2 ion current measured by QMS accelerates toward saturation. The E_a in the k_2 stage below 800 °C at 2 and 5 % O_2 were 178.4 and 174.7 kJ/mol, which were in proximity to the diffusion-controlled E_a value reported by Shimada [9] with 180 kJ/mol at above 470 °C and surface reaction-controlled E_a reported by Barnier [14] with 186 kJ/mol. The E_a in the k_3 stage below 800 °C at 2 % O_2 was 76.6 kJ/mol. This value aligned with the chemical reaction-controlled E_a value of 70.1 kJ/mol reported by Kuriakose [16].

3.3. Oxidation and passivation mechanisms

Generally, oxidation of ZrC initially exhibits k_1 parabolic, followed by k_2 intermediate before transforming into k_3 linear kinetics. However, for temperatures above 800 °C, owing to the considerable amount of CO_2 formation in the beginning of oxidation, the stage enters k_2 oxidation immediately instead of k_1 oxidation. The oxidation and passivation mechanisms in temperature range 600–1000 °C are illustrated in Fig. 9.

k_1 stage: The compact oxide layer thickens parabolically which serves as a barrier for the diffusion of oxygen. The local oxygen activity becomes so low that the amorphous carbon cannot be oxidized while Zr is oxidized, leaving carbon in the dense oxide layer.

k_2 stage: Cracks begin to appear due to the oxidation of amorphous carbon turning into CO_2. The through-thickness or GB cracks formed by CO_2 release create pathways for oxygen transport, thereby increasing the overall effective oxygen diffusion coefficient through the oxide layer or grain boundaries.

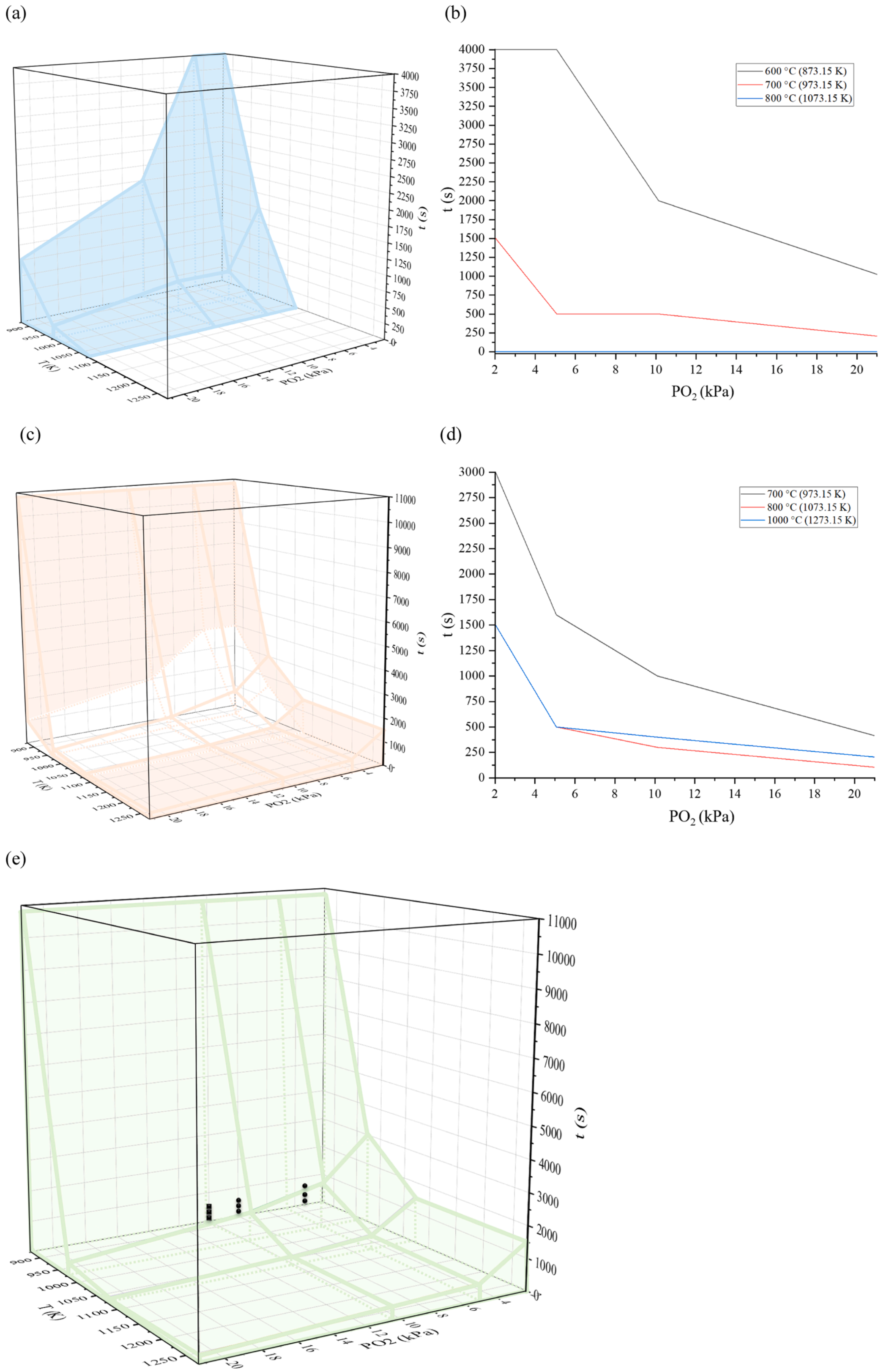

Fig. 6. (a) 3D T-P-t space of k_1 stage (blue). The solid blue boundary lines indicate the k_1-to-k_2 transition boundaries. (b) 2D t-P contour plot of (a) which shows the solid blue transition boundary lines (k_1-to-k_2 transition) in (a). (c) 3D T-P-t space of k_2 stage (orange). The solid orange boundary lines indicate the k_2-to-k_3 transition boundaries. The dotted orange lines delineating the uncolored region inside the orange space indicate the k_1-to-k_2 transition boundaries. (d) 2D t-P contour plot of (c) which shows the solid orange transition boundary lines (k_2-to-k_3 transition) in (c). (e) 3D T-P-t space of $k_1 + k_2$ stages (green). k_3 stage is outside the green space of (e). Kinetic data from ●: Shimada et al. [9]; ■: Barnier et al. [14] lies within the green space showing parabolic oxidation, while Rao et al. [15] and Gasparrini et al. [17] lies outside the green space exhibiting linear oxidation.

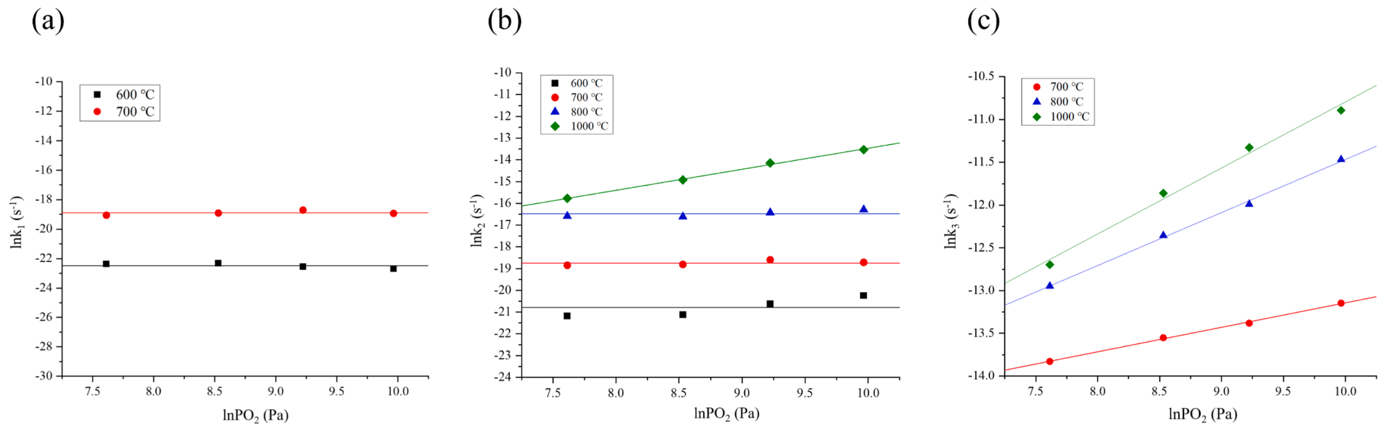

Fig. 7. $\ln k$-$\ln PO_2$ graphs. (a) k_1 (b) k_2 (c) k_3.

Table 4
Summary of the oxidation rate constants (s^{-1}).

	2 % O_2			5 % O_2			10 % O_2			21 % O_2		
600 °C	k_1	k_2		k_1	k_2		k_1	k_2		k_1	k_2	
	1.96E−10	6.31E−10		2.04E−10	6.76E−10		1.62E−10	1.11E−09		1.42E−10	1.63E−09	
700 °C	k_1	k_2	k_3	k_1	k_2	k_3	k_1	k_2	k_3	k_1	k_2	k_3
	5.30E−09	6.53E−09	9.87E−7	6.13E−09	6.80E−09	1.30E−6	7.53E−09	8.39E−09	1.55E−6	5.99E−09	7.47E−09	1.95E−6
800 °C	k_2	k_3		k_2	k_3		k_2	k_3		k_2	k_3	
	6.23E−08	2.39E−06		6.06E−08	4.31E−06		7.36E−08	6.20E−06		8.44E−08	1.05E−05	
1000 °C	k_2	k_3		k_2	k_3		k_2	k_3		k_2	k_3	
	1.41E−07	3.06E−06		3.32E−07	7.06E−06		7.18E−07	1.20E−05		1.33E−06	1.86E−05	

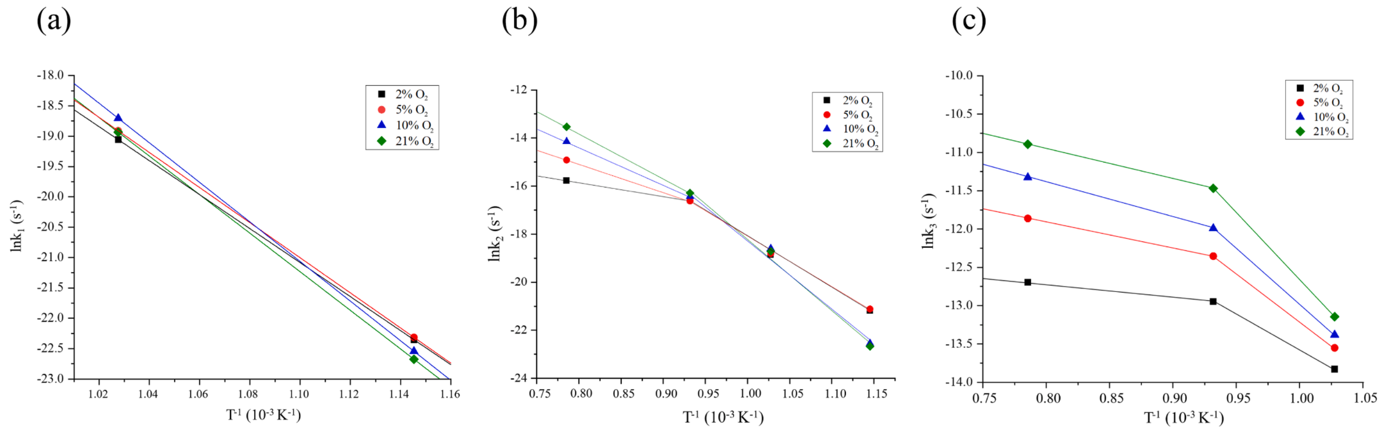

Fig. 8. Arrhenius plots of (a) k_1, (b) k_2, and (c) k_3.

Table 5
E_a (kJ·mol^{-1}) in the parabolic k_1, intermediate k_2, and linear k_3 stage.

	k_1 stage	k_2 stage		k_3 stage	
	Below 700 °C	Below 800 °C	Above 800 °C	Below 800 °C	Above 800 °C
2 % O_2	232.8	178.4	46.5	76.6	14.2
5 % O_2	240.4	174.7	96.6	103.9	27.9
10 % O_2	271.2	239.8	129.4	120.6	37.7
21 % O_2	264.2	249.9	156.5	145.6	32.7

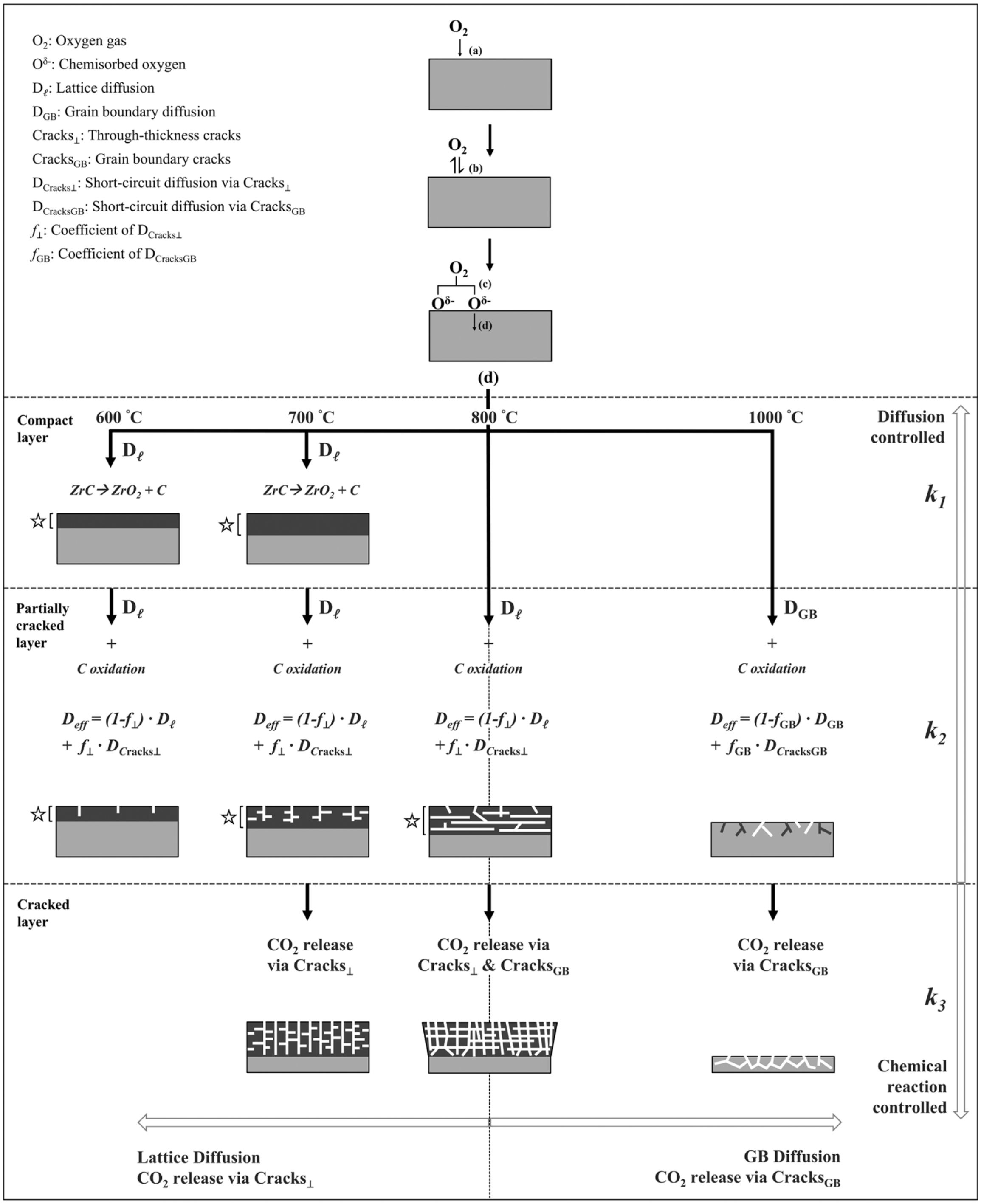

Fig. 9. T-P-t dependent oxidation and passivation mechanisms of SPS-sintered ZrC. (a) Oxygen impingement, (b) Oxygen physisorption, (c) Oxygen dissociative chemisorption, (d) Oxygen inward diffusion. ☆: Passivation layer.

k_3 stage: Increased crack formation enhances diffusion greatly through short-circuit pathways. Through-thickness cracks propagate completely through the thickness of oxide layer (below 800°C) or cracks penetrate most of the GB (above 800°C) near the carbide surface. This eventually leads to chemical reaction to become the final rate-determining step and the observed linear oxidation behavior in many previous studies [16,17,26,27].

The passivation mechanism of SPS-sintered ZrC is mostly due to the delayed carbon oxidation compared to that of zirconium, as observed mostly pronounced at temperatures below 700 °C. This delayed carbon oxidation, as observed from the QMS curves (Fig. 1(a) and Fig. 2(a)), causes significant amount of amorphous carbon to remain in the compact scale (see SAEDP in Supplementary: Figure S3 (f), and Raman spectra in Supplementary: Figure S6). Due to limited CO_2 formation and subsequent through-thickness crack formation, no short-circuit pathways of oxygen transport compromise the protectiveness of the compact oxide scale. To enhance the passivation ability of ZrC against oxidation, it is therefore crucial to reduce the carbon activity in the system, for example, by tuning the C/Zr stoichiometric ratio in ZrC.

4. Conclusions

A thorough and consistent investigation of the oxidation behavior of SPS-sintered ZrC UHTC was performed under various temperature (600–1000 °C) and oxygen pressure (2.0–21.0 % O_2) ranges. By combining TGA and QMS data, we were able to map out the different oxidation stages of SPS-sintered ZrC in 3D T-P-t space for the first time, which offered good comparison to various literature studies of other forms of ZrC (powdered [9,13–15], hot-pressed [17], and electron beam melted [16]). This study also uncovered the underlying mechanism of passivation of ZrC, namely a delayed carbon oxidation compared to zirconia formation, which successfully inhibited the growth of through-thickness and grain boundary cracks. This study highlights the following five key insights into the oxidation and passivation of ZrC ceramic:

(1) Comparison with oxidation behavior of powdered ZrC

Compared to powdered ZrC [9,13–15], for which no grain boundary diffusion has been reported during oxidation, significant grain boundary diffusion occurs in SPS-sintered ZrC oxidized at temperatures above 800 °C.

(2) Fully protective k_1 stage in the 3D T-P-t space

The fully protective k_1 stage was attributed to the carbon retention in the compact oxide scale of SPS-sintered ZrC at temperatures near and below 700 °C, where limited CO_2 formation occurred, as confirmed by QMS. TEM and SAED analyses indicated that the predominant reactions in the k_1 stage were likely as follows:

$$ZrC + \frac{1}{2}(1-x)O_{2(g)} \rightarrow ZrC_xO_{1-x} + (1-x)C$$

$$ZrC + \frac{1}{2}(2-x)O_{2(g)} \rightarrow ZrO_{2-x} + C$$

While the carbon retention phenomenon was also discovered in powdered ZrC, a noticeably larger fully protective k_1 stage was systematically mapped out for the first time.

(3) Two competing mechanisms in ZrC oxidation

The carbon retention and carbon reaction ($C + O_{2(g)} \rightarrow CO_{2(g)}$) mechanisms are separate and parallel during SPS-sintered ZrC oxidation. Carbon retention exists at the initial oxidation stage and promotes compact layer formation, which leads to diffusion-controlled mechanism and parabolic oxidation. Carbon reaction becomes more significant over time, and the formed CO_2 eventually cracks through the scale, forcing the transition to a chemical reaction-controlled mechanism and thus linear oxidation. This study presents the first identification of the transition boundaries in the 3D T-P-t space and 2D t-P projection that delineate the regimes of carbon retention and carbon reaction.

(4) Different E_a under different T and P ranges

In the k_1 stage, E_a was independent of oxygen pressure with oxygen self-diffusion the controlling mechanism. In the k_2 stage, E_a decreased due to the formation of short circuits. In the k_3 stage, E_a dropped to the lowest value due to the transition from diffusion to chemical reaction-controlled mechanism. A pronounced oxygen pressure dependence of E_a was observed in the k_3 stage, confirming that diffusion was no longer the rate-controlling step.

(5) Lattice / grain boundary diffusion dependence on temperature

Enhanced grain boundary diffusion in SPS-sintered ZrC was observed at temperatures of 800 °C and above, as evidenced by SEM analysis. Furthermore, from the Arrhenius plot, an obvious turning point was discovered at 800 °C across all examined oxygen pressures.

These findings could set a foundation for future oxidation studies and oxidation resistance improvement on carbides and UHTCs. For instance, the C/Zr stoichiometry would be a critical parameter to tune for minimizing CO_2 formation while simultaneously stabilizing the carbide phase. In addition, the average grain size and grain boundary characteristics of ZrC would also be crucial features to optimize, particularly under high-temperature oxidation conditions exceeding 800 °C.

CRediT authorship contribution statement

Yun-Ching Lin: Writing – review & editing, Writing – original draft, Visualization, Validation, Methodology, Investigation, Formal analysis, Data curation, Conceptualization. **Hans Brouwer:** Validation, Resources, Methodology, Investigation. **Vera Popovich:** Writing – review & editing, Supervision, Resources. **Yinglu Tang:** Writing – review & editing, Validation, Supervision, Project administration, Methodology, Funding acquisition, Conceptualization.

Declaration of Competing Interest

The authors declare that they have no known competing financial interests or personal relationships that could have appeared to influence the work reported in this paper.

Acknowledgements

For the Titan TEM results in the Supplementary Information, we acknowledge support from the Kavli Institute of Nanoscience, Delft University of Technology, and the Netherlands Electron Microscopy Infrastructure (NEMI), project number 184.034.014, part of the National Roadmap and financed by the Dutch Research Council (NWO).

Appendix A. Supporting information

Supplementary data associated with this article can be found in the online version at doi:10.1016/j.jeurceramsoc.2025.117757.

References

[1] H.F. Jackson, W.E. Lee, Properties and characteristics of ZrC, Compr. Nucl. Mater. 2 (2012) 339–372.

[2] H.O. Pierson, Handbook of rEfractory Carbides and Nitrides: Properties, Characteristics, Processing and Applications, Noyes Publications, 1996.

[3] B.C. Wyatt, S.K. Nemani, G.E. Hilmas, E.J. Opila, B. Anas, Ultra-high temperature ceramics for extreme environments, Nat. Rev. Mater. 9 (2024) 773–789.

[4] F. Frank, M. Tkadletz, C. Saringer, A. Stark, N. Schell, M. Deluca, C. Czettl, N. Schalk, In-situ investigation of the oxidation behaviour of chemical vapour deposited Zr(C,N) hard coatings using synchrotron X-ray diffraction, Coatings 11 (264) (2021).

[5] Y. Katoh, G. Vasudevamurthy, T. Nozawa, L.L. Snead, Properties of zirconium carbide for nuclear fuel applications, J. Nucl. Mater. 441 (2013) 718–742.

[6] X.-M. Hou, K.-C. Chou, Investigation of the effects of temperature and oxygen partial pressure on oxidation of zirconium carbide using different kinetics models, J. Alloy. Compd. 509 (2011) 2395–2400.

[7] A. Bellucci, D. Gozzi, T. Kimura, T. Noda, S. Otani, Zirconia growth on zirconium carbide single crystals by oxidation, Surf. Coat. Technol. 197 (2005) 294–302.

[8] S. Shimada, M. Yoshimatsu, M. Inagaki, S. Otani, Formation and characterization of carbon at the ZrC/ZrO_2 interface by oxidation of ZrC single crystals, Carbon 36 (7-8) (1998) 1125–1131.

[9] S. Shimada, T. Ishii, Oxidation kinetics of zirconium carbide at relatively low temperatures, J. Am. Ceram. Soc. 73 (10) (1990) 2804–2808.

[10] S. Shimada, A thermoanalytical study on the oxidation of ZrC and HfC powders with formation of carbon, Solid State Ion. 149 (3–4) (2002) 319–326.

[11] D. Gozzi, M. Montozzi, P.L. Cignini, Oxidation kinetics of refractory carbides at low oxygen partial pressures, Solid State Ion. 123 (1999) 11–18.

[12] K.R. Janowski, R.D. Carnahan, and R.C. Rossi, Static and Dynamic Oxidation of ZrC, Aerospace Corp., El Segundo, CA, Report no. TDR-669(6250-10)-3, 1966.

[13] R.W. Bartlett, M.E. Wadsworth, I.B. Cutler, The oxidation kinetics of zirconium carbide, Trans. AIME 227 (1963) 467–472.

[14] P. Barnier, F. Thevenot, Comparative study of the oxidation resistance of zirconium carbide and zirconium oxycarbide, Eur. J. Solid State Inorg. Chem. 25 (1988).

[15] G.A. Rama Rao, V. Venugopal, Kinetics and mechanism of the oxidation of ZrC, J. Alloy. Compd. 206 (1994) 237–242.

[16] A.K. Kuriakose, J.L. Margrave, The oxidation kinetics of zirconium diboride and zirconium carbide at high temperatures, J. Electrochem. Soc. 111 (1964) 827.

[17] C. Gasparrini, R.J. Chater, D. Horlait, L. Vandeperre, W.E. Lee, Zirconium carbide oxidation: kinetics and oxygen diffusion through the intermediate layer, J. Am. Ceram. Soc. 101 (2018) 2638–2652.

[18] M.T. Konnik, T. Oldham, A. Rzepka, V. Le Maout, K.A. Stephani, F. Panerai, High-temperature oxidation and nitridation of substoichiometric zirconium carbide in isothermal air, J. Eur. Ceram. Soc. 44 (2024) 6771–6776.

[19] M.T. Konnik, T. Oldham, F. Panerai, K.A. Stephani, The effect of nitrogen on the isothermal oxidation of substoichiometric zirconium carbide: microstructural and spectroscopic investigations, Ceram. Int. 50 (2024) 26596–26606.

[20] D. Sciti, M. Nygren, Spark plasma sintering of ultra refractory compounds, J. Mater. Sci. 43 (2008) 6414–6421.

[21] X. Wei, C. Back, O. Izhvanov, C.D. Haines, E.A. Olevsky, Zirconium carbide produced by spark plasma sintering and hot pressing: densification kinetics, grain growth, and thermal properties, Materials 9 (2016) 577.

[22] B. Ke, W. Ji, J. Zou, W. Wang, Z. Fu, Densification mechanism, microstructure and mechanical properties of ZrC ceramics prepared by high-pressure spark plasma sintering, J. Eur. Ceram. Soc. 43 (2023) 3053–3061.

[23] S. Shimada, Interfacial reaction on oxidation of carbides with formation of carbon, Solid State Ion. 141–142 (2001) 99–104.

[24] C. Gasparrini, R. Podor, D. Horlait, R. Chater, W.E. Lee, Zirconium carbide oxidation: Maltese cross formation and interface characterization, Oxid. Met. 88 (2017) 509–519.

[25] P. Kofstad, High Temperature Corrosion, Elsevier Applied Science Publishers LTD, London, UK, 1988, pp. 171–173.

[26] R.F. Voitovich, E.A. Pugach, High-temperature oxidation of ZrC and HfC, Sov. Powder Metall. Met. Ceram. 12 (1973) 916.

[27] M.M. Opeka, I.G. Talmy, E.J. Wuchina, J.A. Zaykoski, S.J. Causey, Mechanical, thermal, and oxidation properties of refractory hafnium and zirconium compounds, J. Eur. Ceram. Soc. 19 (1999) 2405–2414.